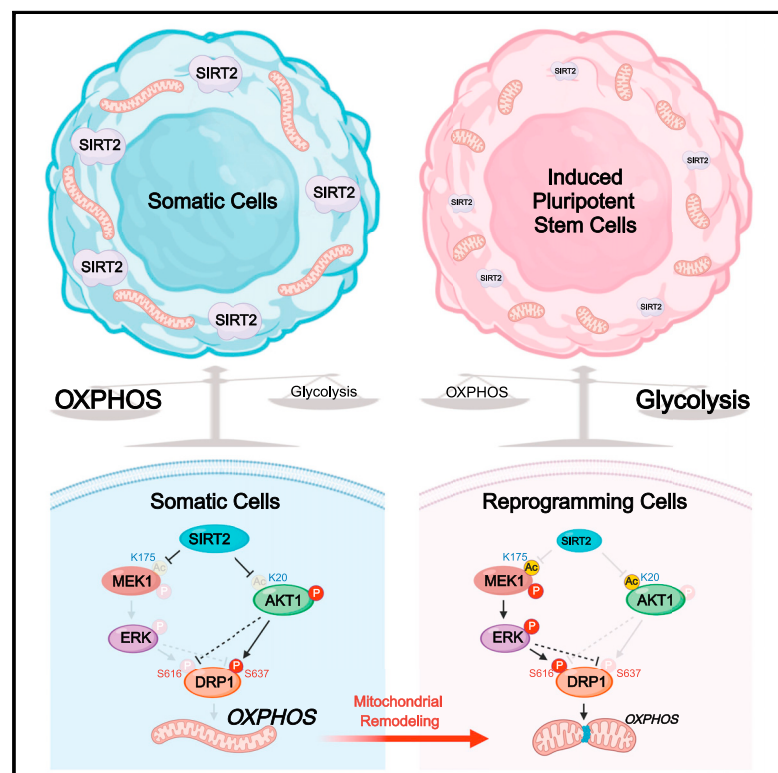**Report**

SIRT2 regulates mitochondrial dynamics and reprogramming via MEK1-ERK-DRP1 and AKT1-DRP1 axes

Graphical abstract

Authors

Young Cha, Taewoo Kim, Jeha Jeon, ..., Pierre Leblanc, Bruce M. Cohen, Kwang-Soo Kim

Correspondence

ycha@mclean.harvard.edu (Y.C.), kskim@mclean.harvard.edu (K.-S.K.)

In brief

Mitochondrial remodeling has critical roles for the somatic cell reprogramming process. Cha et al. report the functional role of SIRT2 in mitochondrial dynamics and remodeling during the human somatic cell reprogramming process. They identify two axes, SIRT2-MEK1-ERK-DRP1 and SIRT2-AKT1-DRP1, that link SIRT2 downregulation to mitochondrial remodeling and somatic cell reprogramming.

Highlights

- SIRT2 regulates DRP1-dependent mitochondrial remodeling in human fibroblasts

- SIRT2KD acetylates MEK1 and activates DRP1-dependent mitochondrial remodeling

- SIRT2KD acetylates AKT1, leading to DRP1-dependent mitochondrial remodeling

- SIRT2 regulates human somatic cell reprogramming via MEK1-ERK and AKT1 axes

Cell Reports

Report

SIRT2 regulates mitochondrial dynamics and reprogramming via MEK1-ERK-DRP1 and AKT1-DRP1 axes

Young Cha,[1,4,*] Taewoo Kim,[1,4] Jeha Jeon,[1] Yongwoo Jang,[1,2] Patrick B. Kim,[1] Claudia Lopes,[1] Pierre Leblanc,[1] Bruce M. Cohen,[3] and Kwang-Soo Kim[1,5,*]

[1]Department of Psychiatry and Molecular Neurobiology Laboratory, McLean Hospital and Program in Neuroscience, Harvard Medical School, Belmont, MA 02478, USA
[2]Department of Biomedical Engineering, Hanyang University, Seoul 04763, Korea
[3]Department of Psychiatry and Program for Neuropsychiatric Research, McLean Hospital, Harvard Medical School, Belmont, MA 02478, USA
[4]These authors contributed equally
[5]Lead contact
*Correspondence: ycha@mclean.harvard.edu (Y.C.), kskim@mclean.harvard.edu (K.-S.K.)
https://doi.org/10.1016/j.celrep.2021.110155

SUMMARY

During somatic reprogramming, cellular energy metabolism fundamentally switches from predominantly mitochondrial oxidative phosphorylation toward glycolysis. This metabolic reprogramming, also called the Warburg effect, is critical for the induction of pluripotency, but its molecular mechanisms remain poorly defined. Notably, SIRT2 is consistently downregulated during the reprogramming process and regulates glycolytic switch. Here, we report that downregulation of SIRT2 increases acetylation of mitogen-activated protein kinase (MAPK) kinase-1 (MEK1) at Lys175, resulting in activation of extracellular signal-regulated kinases (ERKs) and subsequent activation of the pro-fission factor dynamin-related protein 1 (DRP1). In parallel, downregulation of SIRT2 hyperacetylates the serine/threonine protein kinase AKT1 at Lys20 in a non-canonical way, activating DRP1 and metabolic reprogramming. Together, our study identified two axes, SIRT2-MEK1-ERK-DRP1 and SIRT2-AKT1-DRP1, that critically link mitochondrial dynamics and oxidative phosphorylation to the somatic reprogramming process. These upstream signals, together with SIRT2's role in glycolytic switching, may underlie the Warburg effect observed in human somatic cell reprogramming.
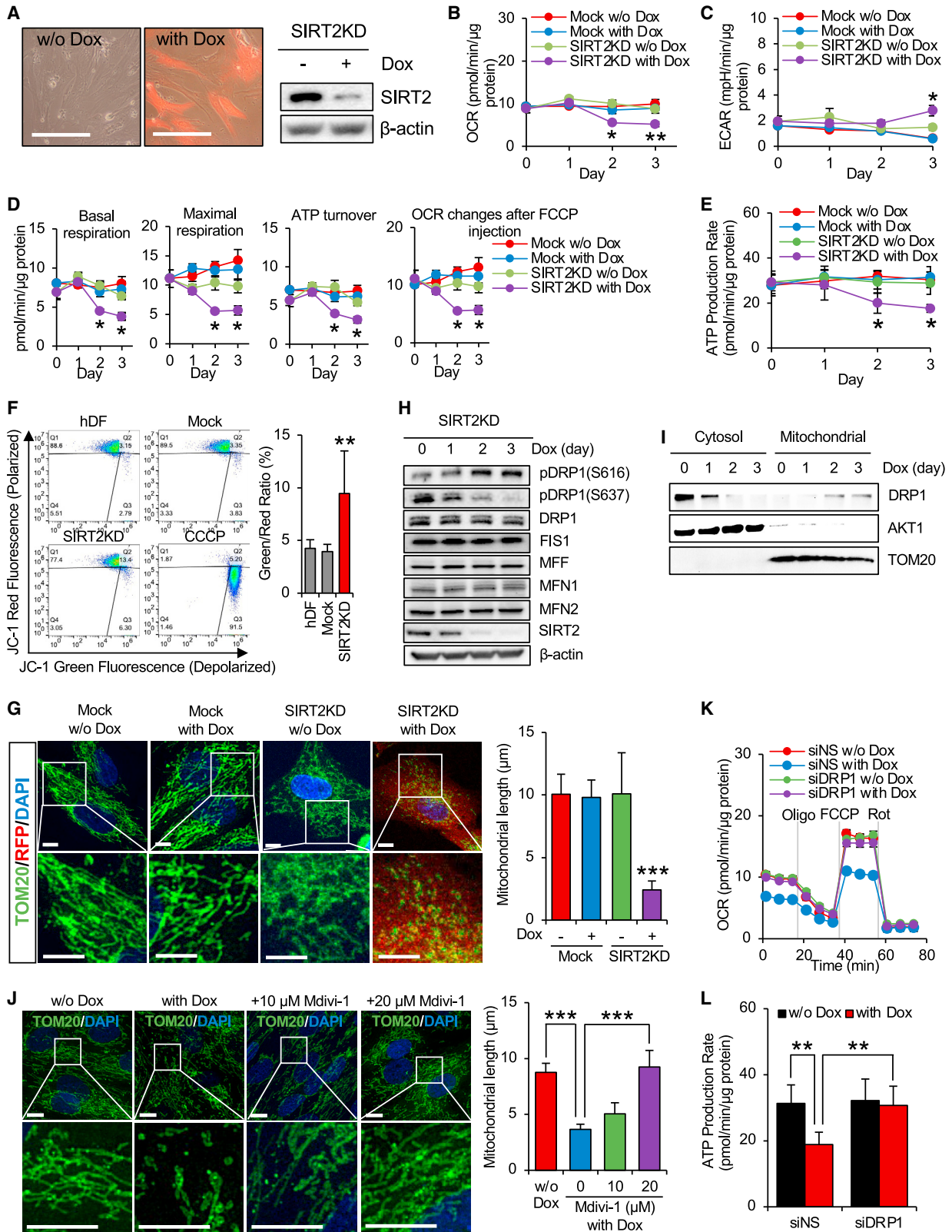
INTRODUCTION

A century ago, German biochemist Otto Warburg reported that cellular metabolism fundamentally switches from mitochondrial oxidative phosphorylation (OXPHOS) to glycolysis when normal cells are transformed to cancer cells (Warburg et al., 1927). This metabolic reprogramming (also called the Warburg effect) has been observed not only in most types of cancers but also in other fast-growing, highly active, or dividing cells such as immune cells (e.g., dendritic and T cells) (Peng et al., 2016; Xu et al., 2021) and diverse stem cells (e.g., embryonic stem cells [ESCs] and induced pluripotent stem cells [iPSCs]) (Folmes et al., 2011; Ito and Suda, 2014). Cellular metabolism has traditionally been viewed as a passive or supportive mechanism of cell fate changes. However, accumulating evidence is changing this perception by showing active roles for metabolism in cell fate decisions. In particular, mitochondria are key organelles linked to the production of ATP and tricarboxylic acid (TCA) cycle metabolites, which play central roles in determining the physiology and metabolism of most eukaryotic cells (Buck et al., 2016; Chakrabarty and Chandel, 2021). In addition, mitochondrial remodeling, through continuous fission and fusion dynamics, has critical

roles not only for tissue homeostatic responses (Archer, 2013) but also for the reprogramming process and maintenance of pluripotency (Chakrabarty and Chandel, 2021). Despite much progress, our understanding of the metabolic reprogramming process is incomplete. For instance, how OXPHOS and glycolysis are regulated in opposite directions in metabolic reprogramming and what initial signals regulate them in conjunction with mitochondrial dynamics have yet to be elucidated.

Sirtuins (SIRTs), which are NAD+-dependent class III histone deacetylases, were originally identified as sensors of cellular energy status and, by controlling acetylation of histones, effectors of gene transcription (Bonkowski and Sinclair, 2016). Mammals have seven SIRT proteins (SIRT1–SIRT7), which reside in distinct subcellular localizations and regulate diverse cellular functions, including physiology, metabolism, and epigenetic regulation (Fang et al., 2019). Among them, SIRT1, SIRT6, and SIRT7 are nuclear proteins, whereas SIRT2 is localized in cytoplasm. SIRT1, the most extensively studied, participates in numerous cellular functions, including lipid metabolism, anti-inflammatory responses, insulin secretion, cell differentiation, and senescence (Colak et al., 2011; Wang et al., 2012). Interestingly, SIRT1 is highly expressed in mouse and human ESCs and critically

(legend on next page)

regulates pluripotency (Williams et al., 2016; Zhang et al., 2014). SIRT6 plays an important role in promoting glucose-stimulated insulin secretion and ATP production in pancreatic β cells and its deficiency is associated with increased lipogenesis and fatty acid uptake, with dysregulation leading to obesity and diabetes (Kuang et al., 2018). SIRT7 regulates DNA repair mechanisms, such as non-homologous end joining, for maintaining genome stability, and SIRT7-deficient mouse models show defective embryogenesis, growth retardation, and reduced lifespan (Fang et al., 2019). SIRT2 is involved in the regulation of metabolic homeostasis, including adipogenesis, fatty acid oxidation, gluconeogenesis, insulin sensitivity, and the inflammatory response (Gomes et al., 2015). SIRT3, SIRT4, and SIRT5 are located in mitochondria and regulate the activity of major metabolic enzymes, participating in the maintenance of mitochondrial functions in response to a variety of physiological conditions (He et al., 2012). Although accumulating evidence indicates critical and diverse roles of SIRTs in metabolism and aging, their functional roles in the balance of glycolysis and OXPHOS, in general, and the Warburg effect, in particular, are poorly understood. Notably, we previously found that SIRT2, the only primarily cytoplasmic SIRT, is consistently downregulated during the reprogramming process, leading to hyperacetylation and activation of major glycolytic enzymes, resulting in increased glycolysis (Cha et al., 2017). In the present study, we report that SIRT2 downregulation suppresses OXPHOS independent of glycolytic increase, demonstrating that SIRT2 controls metabolic reprogramming by regulating both OXPHOS and glycolysis, in opposite directions, during human somatic cell reprogramming. In this regulatory process, SIRT2 targets two axes, the MEK1-ERK-DRP1 and the AKT1-DRP1 pathways, linking mitochondrial remodeling to metabolic reprogramming during the somatic cell reprogramming process.

RESULTS

SIRT2 regulates mitochondrial remodeling and oxidative metabolism via DRP1

We recently observed that SIRT2 downregulation, resulting in hyperacetylation of glycolytic enzymes and enhancement of glycolysis, is a universal signature of human pluripotent stem cells (PSCs) (Cha et al., 2017). However, it is unclear how OXPHOS, the other main source of ATP for energy dependent cell

activities, is regulated during the reprogramming process. Possible mechanisms include (1) glycolytic switch subsequently downregulates OXPHOS by epigenetic mechanism(s); (2) glycolysis and OXPHOS are regulated by separate, independent factors/pathways; and (3) the same factors (e.g., SIRT2) regulate both glycolysis and OXPHOS via distinct pathways. To address these possibilities, we established stable human newborn dermal fibroblast BJ lines (hDFs) expressing SIRT2-specific shRNA and red fluorescent protein (RFP) in a doxycycline (Dox)-inducible manner (Figure 1A). This system provides a useful platform to study the impact of SIRT2 downregulation during the early stages of reprogramming. Notably, Dox-mediated SIRT2 knockdown (KD) robustly influenced mitochondrial oxidative metabolism, as examined by oxygen consumption rate (OCR). As shown in Figures 1B and 1C, SIRT2KD significantly decreased the OCR, reflecting OXPHOS, as early as 2 days after Dox treatment, while the extracellular acidification rate (ECAR), reflecting glycolysis, started to increase at 3 days after Dox treatment, demonstrating that SIRT2KD downregulates OXPHOS ahead of glycolysis upregulation. In addition, SIRT2KD in hDFs resulted in a significant reduction of OXPHOS capacity compared with control cells, as shown by decreases in basal respiration, maximal respiration, and ATP turnover, as well as OCR changes after FCCP treatment (Figures 1D and S1A–S1C). Moreover, compared with control lines, SIRT2KD hDFs displayed significantly decreased cellular ATP production, a functional readout of mitochondrial function (Figure 1E). Furthermore, the levels of mitochondrial TCA cycle metabolites, including citrate, α-ketoglutarate (α-KG), succinate, fumarate, malate, and oxaloacetate (OAA), were significantly reduced in SIRT2KD hDFs compared with control lines (Figures S1D and S1E). We next tested if altered SIRT2 expression affects the mitochondrial membrane potential ($\Delta\Psi_m$). When hDFs were stained with JC-1 fluorescent dye (Smiley et al., 1991), $\Delta\Psi_m$ was significantly downregulated in SIRT2KD hDFs, as shown by higher depolarization (Figure 1F), suggesting that SIRT2KD regulates OXPHOS via mitochondrial remodeling during the early reprogramming process. We next investigated whether altered expression of SIRT2 influences mitochondrial morphology in hDFs. Interestingly, SIRT2KD significantly shortened mitochondrial length by ~70%, compared with control (Figure 1G), which was confirmed by transmission electron microscopy (Figure S1F). The mitochondrial remodeling by SIRT2KD was not

Figure 1. SIRT2 regulates DRP1-dependent mitochondrial oxidative metabolism in hDFs
(A) Left: representative images of inducible SIRT2KD BJ hDFs. Scale bar, 100 μm. Right: western blot analysis for knockdown efficiency of SIRT2.
(B and C) OCR (B) and ECAR (C) levels of mock and inducible SIRT2KD BJ hDFs (n = 5).
(D) Comparison of OXPHOS capacity from mock and SIRT2KD (n = 5).
(E) Comparison of ATP production rates from mock and inducible SIRT2KD BJ hDFs (n = 6).
(F) Left: representative flow cytometry images from mock and SIRT2KD BJ hDFs stained with JC-1 dye. Carbonyl cyanide 3-chlorophenylhydrazone (CCCP) as positive control. Right: quantification of the fluorescence ratio of JC-1 (green/red) from WT, mock, and SIRT2KD BJ hDFs (n = 6).
(G) Left: immunofluorescent images of TOM20 from mock and inducible SIRT2KD BJ hDFs. Scale bar, 10 μm. Right: quantification of mitochondrial length between mock and SIRT2KD (n = 15).
(H) Protein levels of indicated mitochondrial dynamics.
(I) Protein levels of DRP1, AKT1, and TOM20 from cytosolic or mitochondrial fractions.
(J) Left: representative images showing effects of Mdivi-1 on mitochondrial morphology. Scale bar, 10 μm. Right: quantification of mitochondrial length from SIRT2KD BJ hDFs treated with Mdivi-1 (n = 15).
(K and L) OXPHOS capacity (K) and ATP production rate (L) of siNS or siDRP1 transfected inducible SIRT2KD BJ hDFs at 3 days post transfection (n = 6). Data are represented as mean ± SD, *p < 0.05; **p < 0.01; ***p < 0.005. See also Figure S1.
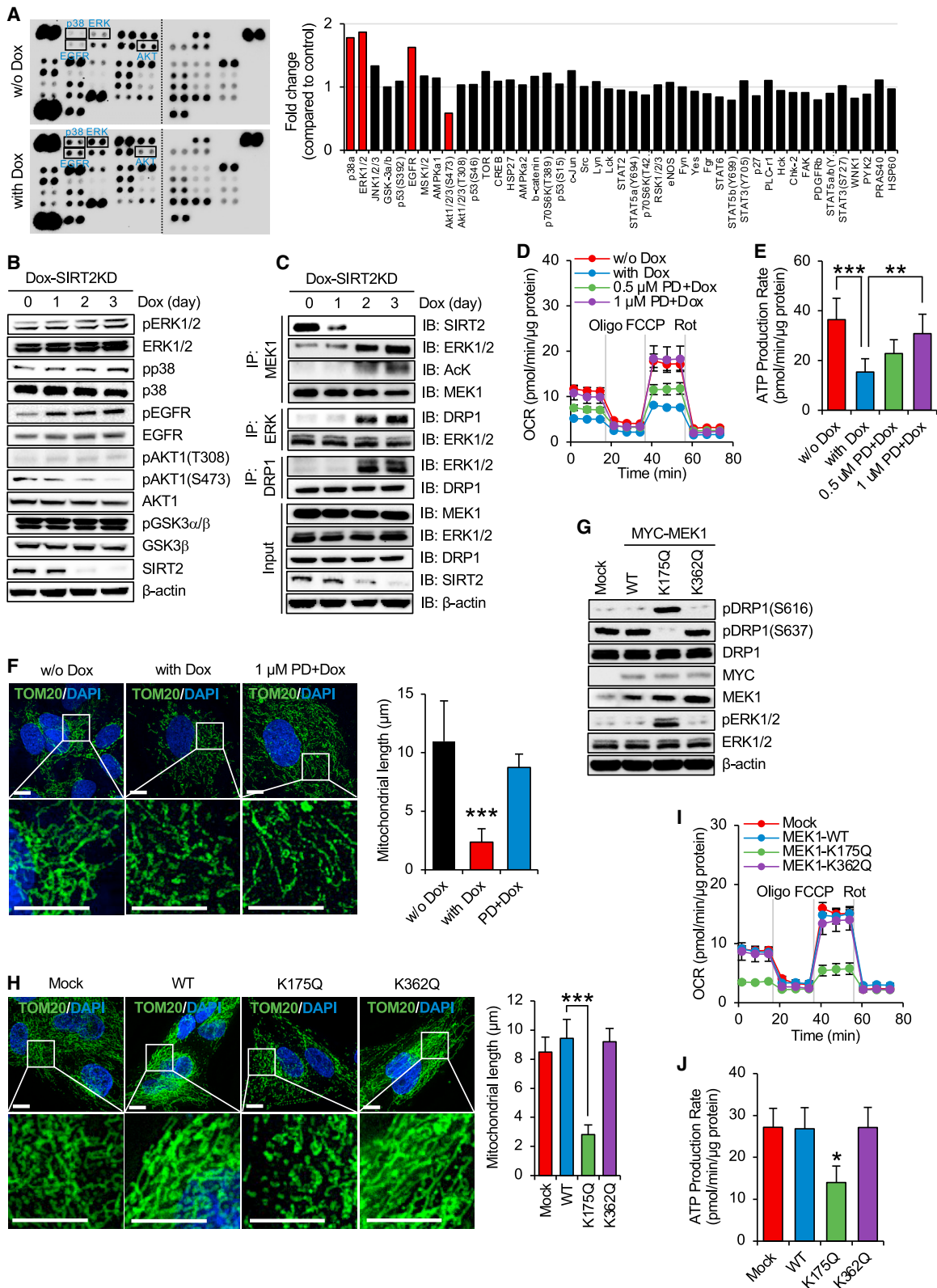
(legend on next page)

associated with apoptosis (Figure S1G). Taken together, these data strongly support that SIRT2 controls OXPHOS metabolism via mitochondrial remodeling, independent of its control of glycolysis.

To understand how SIRT2 regulates mitochondrial dynamics, we tested whether SIRT2 regulates expression of key mitochondrial dynamics factors, regulating fission (e.g., dynamin-related protein 1 [DRP1], mitochondrial fission 1 protein [FIS1], and mitochondrial fission factor [MFF]) or fusion (e.g., mitofusin 1 [MFN1], and MFN2) (Archer, 2013), but failed to find any significant changes in expression levels of mRNAs and proteins for these factors (Figures 1H and S1H). Since SIRT2KD prominently shortened mitochondrial length (Figure 1G), we tested whether SIRT2 affects the phosphorylation levels of pro-fission factor DRP1. Remarkably, SIRT2KD prominently increased phosphorylation of DRP1 at S616 and decreased phosphorylation at S637 (Figure 1H). Because phosphorylation at S616 and S637, respectively, are known to activate and inhibit the function of DRP1 (Archer, 2013), SIRT2KD seems to effectively modulate DRP1's function by regulating the phosphorylation of these residues in opposite directions. In addition, DRP1 activated by SIRT2KD was translocated to mitochondria (Figure 1I). Treatment with 20 μM Mdivi-1, a DRP1 inhibitor (Tanaka and Youle, 2008), efficiently restored the fragmented mitochondrial network and the reduced mitochondrial mass by SIRT2KD without any cytotoxicity (Figures 1J, S1I, and S1J). Furthermore, DRP1KD, using its specific small interfering RNA (siRNA), restored the reduced oxidative metabolism by SIRT2KD to the level of control cells (Figures 1K, 1L, and S1K–S1M), suggesting that SIRT2 regulates OXPHOS via mitochondrial remodeling in a DRP1-dependent manner.

SIRT2 regulates mitochondrial remodeling and oxidative metabolism via the MEK1-ERK-DRP1 axis

How does SIRT2 regulate DRP1? SIRT2 is a cytosolic NAD$^+$-dependent deacetylase (Bonkowski and Sinclair, 2016). Since it has no known kinase activity, we speculated that it indirectly regulates DRP1 phosphorylation levels. In line with this mechanism, no direct interaction between SIRT2 and DRP1 was observed (Figure S2A). To address if kinase(s) are intermediate effector(s) of the SIRT2-DRP1 pathway, we performed a phospho-kinase array on SIRT2KD hDFs with or without Dox, and found that phosphorylation levels of extracellular signal-regulated kinases (ERKs; also known as mitogen-activated protein kinases [MAPKs]), p38 MAPK (p38), and epidermal growth factor receptor (EGFR) were strongly upregulated by SIRT2KD, whereas AKT1 phosphorylation level was downregulated in

SIRT2KD, compared with control (Figure 2A). These findings were confirmed by western blot data showing SIRT2KD-driven hyper-phosphorylation of ERK, p38, and EGFR, and de-phosphorylation of AKT at S473 (Figure 2B). To investigate the functional link between phosphorylation of ERK, p38, or EGFR and DRP1 activation by SIRT2KD, we tested the effects of specific inhibitors of the MEK-ERK axis (PD0325901; PD) (Henderson et al., 2010), p38 (SB202190; SB) (Nemoto et al., 1998), and EGFR (OSI-744; OSI) (Moyer et al., 1997). Notably, treatment with PD, but not with SB or OSI, prominently reversed the effect of SIRT2KD on DRP1 by dephosphorylating S616 and phosphorylating S637 residues (Figures S2B–S2D). Thus, we focused on the functional role of ERK. Immunoprecipitation analyses demonstrated that interaction between ERK and DRP1 was robustly increased by SIRT2KD (Figure 2C). Furthermore, PD treatment reversed the decreased OXPHOS capacity and ATP production as well as reducing mitochondrial length changes caused by SIRT2KD (Figures 2D–2F and S2E), demonstrating that SIRT2 regulates mitochondrial OXPHOS via the ERK-DRP1 axis. To exclude the possibility that this was a cell-line-specific effect, we repeated our experiments in an independent adult hDF line, GM03529, and replicated our results (Figures S2F and S2G). However, we failed to observe direct interaction between SIRT2 and ERK (Figure S2A), prompting us to hypothesize that there could be another mediator between SIRT2 and ERK. Since MAPK kinase-1 (MEK1) is known to act upstream of ERK (Crews et al., 1992), we tested whether MEK1 is involved. We found that the acetylation levels of MEK1 are very low when SIRT2 levels are adequate (day 0 or 1; Figure 2C). SIRT2 downregulation by Dox treatment (day 2 or 3) resulted in hyper-acetylation of MEK1, facilitating its interaction with ERK1/2 and hyperphosphorylation of ERK1/2 (Figure 2C). Since a previous study showed that K175 and K362 of MEK1 are effectively acetylated by p300 histone acetyltransferase and deacetylated by SIRT1 or SIRT2 (Yeung et al., 2015), we tested whether acetylation of K175 and K362 is functionally involved. Both K175 and K362 residues are highly conserved among diverse species (Figure S2H), and a structural model of MEK1 showed that both residues are exposed to the outside surface of MEK1 (Figure S2I). We mutated each residue to glutamine (an acetylation mimetic) and examined the effects on DRP1 phosphorylation. Interestingly, MEK1-K175Q, but not MEK1-K362Q, greatly influenced the phosphorylation status of DRP1 by phosphorylating S616 and dephosphorylating S637 residues (Figure 2G). Furthermore, ectopic expression of MEK1-K175Q, but not MEK1-K362Q, prominently induced mitochondrial fission (Figure 2H) and

Figure 2. SIRT2 controls DRP1-dependent mitochondrial fission by regulating the MEK1-ERK axis
(A) Left: phospho-kinase screen in SIRT2KD BJ hDFs with or without Dox for 3 days. Right: relative intensities of the phospho-kinase spots.
(B) Western blot analysis of inducible SIRT2KD BJ hDFs.
(C) Western blot analyses of MEK1, ERK1/2, or DRP1-immunoprecipitated lysates from inducible SIRT2KD BJ hDFs.
(D and E) Effects of PD on OXPHOS capacity (D) and ATP production rate (E) from inducible SIRT2KD BJ hDFs with or without Dox (n = 6).
(F) Left: representative images showing effects of PD on mitochondrial morphology. Scale bar, 10 μm. Right: quantification of mitochondrial length and/or PD (n = 11).
(G) Western blot analyses on the effects of MEK1-WT, MEK1-K175Q, and MEK1-K362Q on DRP1 activity.
(H) Left: representative images of mitochondrial morphology by MEK1-WT, MEK1-K175Q, and MEK1-K362Q. Scale bar, 10 μm. Right: quantification of mitochondrial length from MEK1-WT, MEK1-K175Q, and MEK1-K362Q transfected WT BJ hDFs (n = 6).
(I and J) OXPHOS capacity (I) and ATP production rate (J) from MEK1-WT, MEK1-K175Q, and MEK1-K362Q transfected WT BJ hDFs (n = 3). Data are represented as mean ± SD, *p < 0.05; **p < 0.01; ***p < 0.005. See also Figure S2.
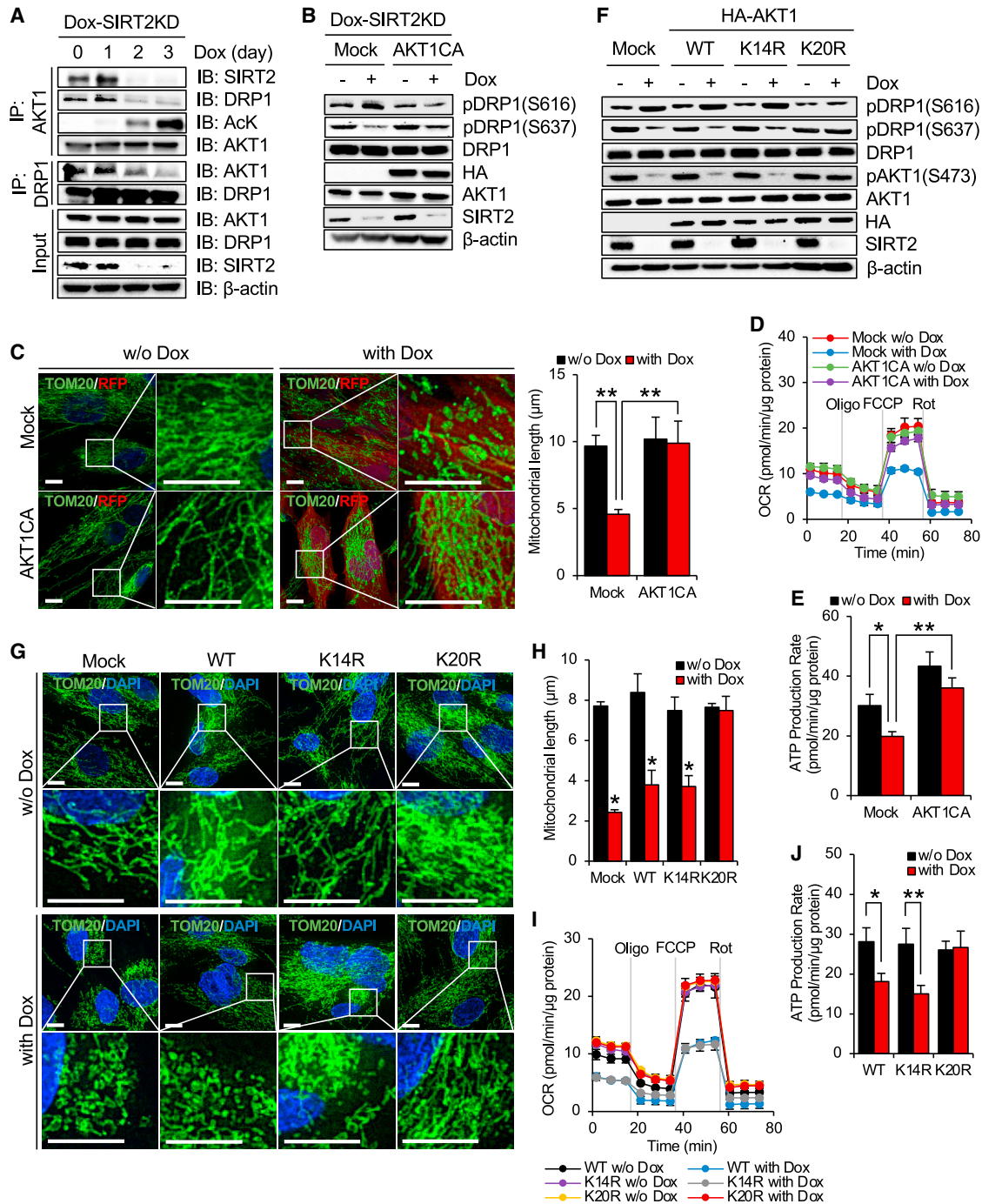
Figure 3. SIRT2 regulates oxidative metabolism by activating AKT1

(A) Total protein extracts were immunoprecipitated using anti-AKT1 or anti-DRP1 antibodies and western blotting was performed with whole-cell lysate (input) as control of equal protein concentration for immunoprecipitation.

(B) Effects of AKT1CA on DRP1 activity.

(C) Left: representative images showing effects of AKT1CA on mitochondrial length. Scale bar, 10 μm. Right: quantification of mitochondrial length affected by AKT1CA (n = 14).

(D and E) OXPHOS capacity (D) and ATP production rate (E) from AKT1CA transfected hDFs (n = 6).

(F) Western blot analyses showing on the effects of AKT1-WT, AKT1-K14R, and AKT1-K20R on DRP1 activity.

(G) Representative images of mitochondrial morphology from AKT1-WT, AKT1-K14R, and AKT1-K20R transfected SIRT2KD BJ hDFs. Scale bar, 10 μm.

(legend continued on next page)

decreased OXPHOS capacity and ATP production (Figures 2I, 2J, and S2J–S2M). Moreover, MEK1-K175Q, but not wild-type (WT) or MEK1-K362Q, significantly reduced the production of citrate, α-KG, malate, and OAA (Figure S2N). Identical results were obtained in both BJ (Figures 2A–2J, S2A–S2E, S2J, and S2N) and GM03529 hDF lines (Figures S2F, S2G, and S2K–S2M). To address whether MEK1-K175Q regulates mitochondrial remodeling and OXPHOS capacity via ERK and DRP1, we tested the effects of specific inhibitors of ERK1 (SCH772984; SCH) (Wong et al., 2014) and DRP1 (Mdivi-1). Notably, treatment with either SCH or Mdivi-1 prominently reversed the reduction of mitochondrial length and OXPHOS capacity caused by MEK1-K175Q (Figures S2O–S2Q). Taken together, these results strongly suggest that SIRT2 regulates mitochondrial dynamics and OXPHOS through the MEK1-ERK-DRP1 axis.

SIRT2 regulates mitochondrial remodeling and oxidative metabolism via the AKT1-DRP1 axis

In our phospho-kinase array analysis, the phosphorylation level of AKT1 at S473 was downregulated in SIRT2KD compared with control (Figure 2A). In canonical AKT signaling, phosphorylation at both serine 473 (S473) and threonine 308 (T308) residues is required for maximal activation (Manning and Toker, 2017). However, SIRT2KD did not affect AKT1 phosphorylation at T308 (Figures 2A and 2B). Also, the phosphorylation level of GSK3α/β, a major AKT substrate (Manning and Toker, 2017), was unaffected by SIRT2KD, suggesting that SIRT2 regulates a non-canonical AKT signaling pathway. We found that the acetylation levels of AKT1 are very low when SIRT2 levels are adequate (day 0 or 1). Then, SIRT2KD leads to prominent hyperacetylation of AKT1 (day 2 or 3), diminishing its interaction with DRP1 (Figure 3A). To directly test AKT1's function on DRP1 activation, we transfected SIRT2KD hDFs with a constitutively active form of AKT1 (AKT1CA) (Ramaswamy et al., 1999) with or without Dox. Notably, ectopic expression of AKT1CA diminished the effects of SIRT2KD on DRP1 phosphorylation (Figure 3B). In addition, AKT1CA overexpression in SIRT2KD hDFs treated with Dox increased mitochondrial length to the level of control cells (Figure 3C) and leads to an increase in OXPHOS capacity and ATP production reduced by SIRT2KD (Figures 3D, 3E, and S3A). The same pattern was observed in GM03529 cells (Figures S3B–S3D). We next sought to identify specific lysine residues of AKT1 that are targeted by SIRT2 and their functional effects. A previous study having identified deacetylation of pleckstrin homology domain residues K14 and K20 by SIRT1 (Sundaresan et al., 2011), we speculated that SIRT2 regulates AKT1 activity through deacetylating K14 and/or K20, which are highly conserved among diverse species (Figure S3E). A structural model showed that both residues are exposed to the outside surface of AKT1, suggesting their availability to interact with SIRT2 (Figure S3F). We generated plasmid vectors expressing acetylation-deficient AKT1 by mutating K14 and K20 to arginine (K14R and K20R, respectively) and examined their activities. We found that SIRT2KD prominently activated DRP1 via phosphor-

ylating S616 and dephosphorylating S637 residues when AKT1-WT or AKT1-K14R was introduced into cells (Figure 3F). In contrast, DRP1 activation by SIRT2KD was completely blocked when AKT1-K20R was introduced. In addition, AKT1-K20R, but not AKT1-WT or AKT1-K14R, prevented mitochondrial fission and completely rescued OCR, and ATP production, in both SIRT2KD BJ and GM03529 hDFs (Figures 3G–3J and S3G–S3J). Furthermore, decreased production of citrate, α-KG, malate, and OAA by SIRT2KD were restored by AKT1-K20R, but not by AKT1-WT or AKT1-K14R (Figure S3K). Together, SIRT2 critically regulates mitochondrial dynamics and OXPHOS via AKT1's K20 deacetylation (Figure 4G).

SIRT2-DRP1 axis regulates human somatic cell reprogramming via both MEK1-ERK and AKT1

To address whether these pathways are critical for the reprogramming process, we first tested the effects of DRP1 inhibition by Mdivi-1 on metabolic reprogramming and human iPSC (hiPSC) generation. To test the effects of Mdivi-1 treatment on metabolic reprogramming, OCR was measured at 8 days post infection (dpi) with the Yamanaka 4 factors (Y4F) (Takahashi and Yamanaka, 2006). Treatment with Mdivi-1 reverted the reduced OXPHOS capacity by SIRT2KD, demonstrating that the metabolic switch from OXPHOS to glycolysis depends on DRP1 (Figures 4A and S4A). When Y4F were introduced into hDFs together with SIRT2KD, generation of iPSC colonies was significantly enhanced, as examined at 16 dpi (Figure 4B). Treatment with Mdivi-1 resulted in decreased generation of iPSC colonies in a dose-dependent manner. Interestingly, 10 μM Mdivi-1 reduced hiPSC generation to the levels observed with Y4F only, suggesting that Mdivi-1 blocks SIRT2KD's reprogramming-enhancing effect (Figure 4B). Furthermore, when hDFs were treated with 20 μM Mdivi-1, SIRT2KD's effect was completely abrogated, showing that DRP1 activation is critical for hiPSC generation (Figure 4B). We next tested whether inhibition of the MEK1-ERK pathway affects hiPSC generation by treatment with a specific inhibitor. Treatment of cells undergoing reprogramming with 1 μM PD robustly enhanced their OXPHOS capacity at early stages of reprogramming (Figures 4C and S4B). Additionally, PD treatment significantly decreased hiPSC generation in a dose-dependent manner (Figure 4D). Finally, we tested whether a deacetylated mimetic of AKT1 influences hiPSC generation from hDFs infected with Y4F together with or without SIRT2KD. Notably, ectopic expression of AKT1-K20R, but not AKT1-WT or AKT1-K14R, enhanced the OXPHOS capacity and inhibited metabolic reprogramming during the early stages of the reprogramming process (Figures 4E and S4C). In addition, AKT1-K20R, but not AKT1-WT or AKT1-K14R, significantly diminished generation of iPSC colonies and completely abolished SIRT2KD's reprogramming-enhancing ability (Figure 4F). In sum, our results support a model in which SIRT2 critically regulates metabolic reprogramming and human pluripotency induction via controlling mitochondrial dynamics by targeting distinct specific pathways: MEK1-ERK-DRP1 and AKT1-DRP1 (Figure 4G).

(H) Quantification of mitochondrial length shown in (G) (n = 6).

(I and J) OXPHOS capacity (I) and ATP production rate (J) from AKT1-WT, AKT1-K14R, and AKT1-K20R transfected SIRT2KD BJ hDFs (n = 3). Data are represented as mean ± SD, *p < 0.05; **p < 0.01. See also Figure S3.
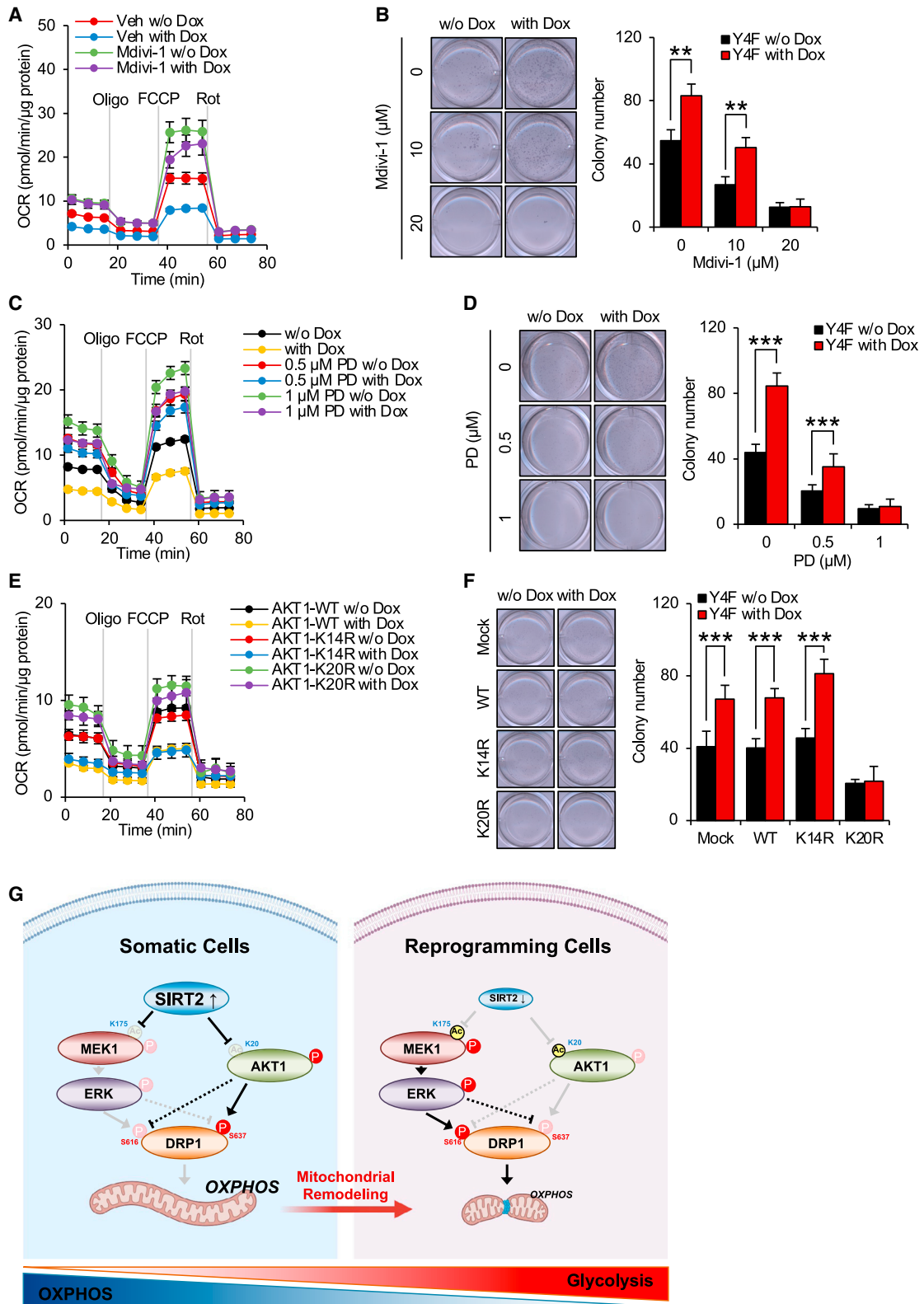
(legend on next page)

DISCUSSION

Since the ground-breaking studies by Dr. Yamanaka and his colleagues showed that terminally differentiated somatic cells can be reprogrammed to iPSCs with indefinite self-renewal and pluripotent differentiation potential (Takahashi and Yamanaka, 2006), numerous laboratories have attempted to delineate the underlying mechanisms of the reprogramming process (Shi et al., 2017; Takahashi and Yamanaka, 2016). One of most salient findings is that, as seen in cancer cells, somatic reprogramming is associated with fundamental changes of cellular metabolism; specifically, a switch from predominance of OXSPHOS to glycolysis, a Warburg effect (Folmes et al., 2011; Panopoulos et al., 2012). Although this metabolic change was initially considered to be an adaptive process, detailed analyses revealed that it precedes and is required for the induction of the intrinsic pluripotent gene network. Notably, these studies also revealed that mitochondrial remodeling is a critical component of the reprogramming process (reviewed in Chakrabarty and Chandel, 2021; Chen and Chan, 2017). For instance, the MAPK phosphatase Dusp6 was downregulated by reprogramming factors, leading to early Erk1/2 phosphorylation/activation and subsequent induction of the pro-fission factor Drp1 in the early process of mouse fibroblast reprogramming (Prieto et al., 2016). In addition, an oocyte-factor, Tcl1, was found to inhibit mitochondrial biogenesis and OXPHOS by mitochondrial polynucleotide phosphorylase (PnPase), leading to the promotion of mouse somatic cell reprogramming into iPSCs (Khaw et al., 2015).

In the present study, we report SIRT2's unexpected role in mitochondrial remodeling and oxidative metabolism reduction during human somatic cell reprogramming (Figure 4G). We discovered that SIRT2 works as an upstream regulator of MEK1 and AKT1 through regulating their acetylation at K175 and K20, respectively. In somatic cells where SIRT2 levels are high, these residues are deacetylated by SIRT2. Deacetylation of MEK1 at K175 inactivates its kinase function, resulting in inactive state for ERK and DRP1. When SIRT2 is downregulated (by its KD or miR-200c during the reprogramming process), MEK1 is acetylated at K175 and becomes active, leading to phosphorylation/activation of ERK. In turn, activated ERK induces DRP1-dependent mitochondrial remodeling through phosphorylating S616 and dephosphorylating S637 residues. In contrast, deacetylated AKT1 at K20 in hDFs works as an efficient repressor of DRP1 by phosphorylating S637 and dephosphorylating S616. Then, its acetylation by SIRT2KD blocks AKT1's repressor function, activating DRP1 function. As a result, SIRT2KD during the reprogram-

ming process effectively activates DRP1 by simultaneously facilitating MEK1's activator and blocking AKT1's repressor function, leading to mitochondrial remodeling and OXPHOS reduction (Figure 4G). Notably, our data show that blocking each signaling pathway completely reverted mitochondrial remodeling by SIRT2KD, which may be explained by our non-physiological overexpression of dominant-negative forms in hDFs. During the reprogramming process, these two pathways likely coordinate together to achieve metabolic and somatic reprogramming.

While AKT1 was shown to be important for maintenance of ESC pluripotency (Armstrong et al., 2006; Watanabe et al., 2006), its role in metabolic reprogramming and its regulation by SIRT2 were unknown. In addition, regulation of MEK1 by SIRT2 in metabolic reprogramming has not been reported. Interestingly, a recent study revealed that lactate dehydrogenase A is critical for metabolic reprogramming in activated T cells through phosphoinositide 3-kinase (PI3K)-AKT signaling (Peng et al., 2016; Xu et al., 2021), where AKT is the canonical pathway with phosphorylation at both T308 and S473 required to produce full activity (Hoxhaj and Manning, 2020). In contrast, SIRT2KD dephosphorylated AKT1 at S473, but not at T308, and did not influence phosphorylation levels of well-known substrates (e.g., GSK-3α/β and mTORC1), strongly supporting the importance of PI3K-independent, non-canonical AKT1 signaling regulated by SIRT2. Similarly, non-canonical AKT1 signaling has been reported in different cellular contexts (Chen et al., 2013; Wan and Helman, 2003). Thus, AKT1 regulation appears to be dependent upon upstream signals and/or cell contexts, and it will be of great interest to further investigate the functional roles of both canonical and non-canonical AKT pathways in producing the Warburg effect in different cellular contexts.

Mitochondrial remodeling seems to be coupled with the Warburg effect not only in the hiPSC reprogramming process but also in mediating cell fate changes of cancer cells and immune cells (Buck et al., 2016; Chen and Chan, 2017). However, it is worthwhile noting that mitochondrial dynamics are divergent in some other fast-dividing cells. For instance, neural stem cells' mitochondria were reported to be in tubular forms, although they also exhibit the Warburg effect (Khacho et al., 2016). In addition, Ludikhuize et al. (2020) recently showed that Lgr5^{+} intestinal stem cells are enriched in mitochondria and their differentiation to linage cells requires mitochondrial fission, which is the opposite of the process observed in the differentiation of hPSCs, requiring mitochondrial fusion. Thus, although it is generally assumed that the Warburg effect accompanies fragmented mitochondria, diverse mechanisms may underlie or be

---

Figure 4. The SIRT2-DRP1 axis regulates human somatic cell reprogramming via both MEK1-ERK and AKT1
(A) Effects of Mdivi-1 on OXPHOS capacity from inducible SIRT2KD BJ hDFs by Y4F at 8 days post infection (dpi) (n = 6).
(B) Effects of Mdivi-1 on hiPSC generation by Y4F and/or SIRT2KD at 16 dpi (n = 4).
(C) Effects of PD on OXPHOS capacity from inducible SIRT2KD BJ hDFs by Y4F at 8 dpi (n = 4).
(D) Effects of PD on hiPSC generation by Y4F and/or SIRT2KD at 16 dpi (n = 8).
(E) Effects of AKT1-mut on OXPHOS capacity from inducible SIRT2KD BJ hDFs by Y4F at 8 dpi (n = 4).
(F) Effects of AKT1-mut on hiPSC generation by Y4F and/or SIRT2KD at 16 dpi (n = 6).
(G) Proposed model for SIRT2-DRP1 axis in regulating mitochondrial remodeling during human somatic cell reprogramming via MEK1-ERK and AKT1 signaling pathway. Data are represented as mean ± SD, **p < 0.01; ***p < 0.005. See also Figure S4.

associated with it in different cellular contexts (Chakrabarty and Chandel, 2021; Chen and Chan, 2017).

Limitations of the study

Using the reprogramming of human dermal fibroblasts as an experimental system, we show evidence that SIRT2 controls mitochondrial dynamics during the early phase of reprogramming by regulating two axes, MEK1-ERK-DRP1 and AKT1-DRP1. Although our results were reproduced in two independent human dermal fibroblast lines, one newborn and one adult, it awaits further confirmation whether the same pathways are involved in the reprogramming process of other species (e.g., mouse) and types of somatic cells (e.g., blood cells). It is unknown whether the pathways observed here regulate metabolic reprogramming to produce a similar Warburg effect in an array of actively growing cell types, such as cancer cells, immune cells, and other types of stem cells. In addition, this study showed that AKT1 and MEK1 can regulate the phosphorylation of two different residues (S616 and S637) of DRP1 in opposite directions. While unidentified kinases/phosphatases may be involved, detailed mechanisms await further investigation. Furthermore, although we found that phosphorylation of AKT1, p38, and EGFR is regulated by SIRT2 expression, their functional role and mechanisms remain unknown. Finally, it will be of great interest whether canonical and non-canonical AKT pathways may have distinct functional roles in mitochondrial remodeling and/or in the reprogramming process in different cellular contexts.

STAR★METHODS

Detailed methods are provided in the online version of this paper and include the following:

- KEY RESOURCES TABLE
- RESOURCE AVAILABILITY
  - Lead contact
  - Materials availability
  - Data and code availability
- EXPERIMENTAL MODEL AND SUBJECT DETAILS
  - Cell lines
- METHOD DETAILS
  - Plasmid construction
  - Lentivirus production
  - Live cell metabolic analysis
  - Measurement of mitochondrial length
  - Mitochondrial function assay
  - Measurement of mitochondrial metabolites
  - Measurement of mitochondrial membrane potential
  - Measurement of mitochondrial mass
  - Transmission electron microscopy
  - Isolation of cytosolic and mitochondrial fractions
  - Phospho-kinase array
  - qRT-PCR
  - Immunoprecipitation
  - Immunoblotting
  - Annexin V staining
  - Cell viability assay
  - Human iPSC formation assay
- QUANTIFICATION AND STATISTICAL ANALYSIS

AUTHOR CONTRIBUTIONS

K.-S.K. and Y.C. conceived and supervised the project; Y.C. and T.K. designed and performed the experiments and analyzed the data. J.J., Y.J., P.B.K., and C.L. performed the experiments. P.L. and B.M.C. analyzed the data. Y.C. and K.-S.K. wrote the manuscript.

REFERENCES

Archer, S.L. (2013). Mitochondrial dynamics—mitochondrial fission and fusion in human diseases. N. Engl. J. Med. *369*, 2236–2251.

Armstrong, L., Hughes, O., Yung, S., Hyslop, L., Stewart, R., Wappler, I., Peters, H., Walter, T., Stojkovic, P., Evans, J., et al. (2006). The role of PI3K/AKT, MAPK/ERK and NFkappabeta signalling in the maintenance of human embryonic stem cell pluripotency and viability highlighted by transcriptional profiling and functional analysis. Hum. Mol. Genet. *15*, 1894–1913.

Bonkowski, M.S., and Sinclair, D.A. (2016). Slowing ageing by design: the rise of NAD+ and sirtuin-activating compounds. Nat. Rev. Mol. Cell Biol. *17*, 679–690.

Buck, M.D., O'Sullivan, D., Klein Geltink, R.I., Curtis, J.D., Chang, C.H., Sanin, D.E., Qiu, J., Kretz, O., Braas, D., van der Windt, G.J., et al. (2016). Mitochondrial dynamics controls T cell fate through metabolic programming. Cell *166*, 63–76.

Cha, Y., Han, M.J., Cha, H.J., Zoldan, J., Burkart, A., Jung, J.H., Jang, Y., Kim, C.H., Jeong, H.C., Kim, B.G., et al. (2017). Metabolic control of primed human pluripotent stem cell fate and function by the miR-200c-SIRT2 axis. Nat. Cell Biol. *19*, 445–456.

Chakrabarty, R.P., and Chandel, N.S. (2021). Mitochondria as signaling organelles control mammalian stem cell fate. Cell Stem Cell *28*, 394–408.

Chen, H., and Chan, D.C. (2017). Mitochondrial dynamics in regulating the unique phenotypes of cancer and stem cells. Cell Metab. *26*, 39–48.

Chen, J., Chan, A.W., To, K.F., Chen, W., Zhang, Z., Ren, J., Song, C., Cheung, Y.S., Lai, P.B., Cheng, S.H., et al. (2013). SIRT2 overexpression in hepatocellular carcinoma mediates epithelial to mesenchymal transition by protein kinase B/glycogen synthase kinase-3beta/beta-catenin signaling. Hepatology *57*, 2287–2298.

Colak, Y., Ozturk, O., Senates, E., Tuncer, I., Yorulmaz, E., Adali, G., Doganay, L., and Enc, F.Y. (2011). SIRT1 as a potential therapeutic target for treatment of nonalcoholic fatty liver disease. Med. Sci. Monit. *17*, HY5–9.

Crews, C.M., Alessandrini, A., and Erikson, R.L. (1992). The primary structure of MEK, a protein kinase that phosphorylates the ERK gene product. Science *258*, 478–480.

Fang, Y., Tang, S., and Li, X. (2019). Sirtuins in metabolic and epigenetic regulation of stem cells. Trends Endocrinol. Metab. *30*, 177–188.

Folmes, C.D., Nelson, T.J., Martinez-Fernandez, A., Arrell, D.K., Lindor, J.Z., Dzeja, P.P., Ikeda, Y., Perez-Terzic, C., and Terzic, A. (2011). Somatic oxidative bioenergetics transitions into pluripotency-dependent glycolysis to facilitate nuclear reprogramming. Cell Metab. *14*, 264–271.

Gomes, P., Fleming Outeiro, T., and Cavadas, C. (2015). Emerging role of sirtuin 2 in the regulation of mammalian metabolism. Trends Pharmacol. Sci. *36*, 756–768.

He, W., Newman, J.C., Wang, M.Z., Ho, L., and Verdin, E. (2012). Mitochondrial sirtuins: regulators of protein acylation and metabolism. Trends Endocrinol. Metab. *23*, 467–476.

Henderson, Y.C., Chen, Y., Frederick, M.J., Lai, S.Y., and Clayman, G.L. (2010). MEK inhibitor PD0325901 significantly reduces the growth of papillary thyroid carcinoma cells in vitro and in vivo. Mol. Cancer Ther. *9*, 1968–1976.

Hoxhaj, G., and Manning, B.D. (2020). The PI3K-AKT network at the interface of oncogenic signalling and cancer metabolism. Nat. Rev. Cancer *20*, 74–88.

Ito, K., and Suda, T. (2014). Metabolic requirements for the maintenance of self-renewing stem cells. Nat. Rev. Mol. Cell Biol. *15*, 243–256.

Khacho, M., Clark, A., Svoboda, D.S., Azzi, J., MacLaurin, J.G., Meghaizel, C., Sesaki, H., Lagace, D.C., Germain, M., Harper, M.E., et al. (2016). Mitochondrial dynamics impacts stem cell identity and fate decisions by regulating a nuclear transcriptional program. Cell Stem Cell *19*, 232–247.

Khaw, S.L., Min-Wen, C., Koh, C.G., Lim, B., and Shyh-Chang, N. (2015). Oocyte factors suppress mitochondrial polynucleotide phosphorylase to remodel the metabolome and enhance reprogramming. Cell Rep. *12*, 1080–1088.

Kuang, J., Chen, L., Tang, Q., Zhang, J., Li, Y., and He, J. (2018). The role of Sirt6 in obesity and diabetes. Front. Physiol. *9*, 135.

Ludikhuize, M.C., Meerlo, M., Gallego, M.P., Xanthakis, D., Burgaya Julia, M., Nguyen, N.T.B., Brombacher, E.C., Liv, N., Maurice, M.M., Paik, J.H., et al. (2020). Mitochondria define intestinal stem cell differentiation downstream of a FOXO/notch axis. Cell Metab. *32*, 889–900 e887.

Manning, B.D., and Toker, A. (2017). AKT/PKB signaling: navigating the network. Cell *169*, 381–405.

Moyer, J.D., Barbacci, E.G., Iwata, K.K., Arnold, L., Boman, B., Cunningham, A., DiOrio, C., Doty, J., Morin, M.J., Moyer, M.P., et al. (1997). Induction of apoptosis and cell cycle arrest by CP-358,774, an inhibitor of epidermal growth factor receptor tyrosine kinase. Cancer Res. *57*, 4838–4848.

Nemoto, S., Xiang, J., Huang, S., and Lin, A. (1998). Induction of apoptosis by SB202190 through inhibition of p38beta mitogen-activated protein kinase. J. Biol. Chem. *273*, 16415–16420.

Panopoulos, A.D., Yanes, O., Ruiz, S., Kida, Y.S., Diep, D., Tautenhahn, R., Herrerias, A., Batchelder, E.M., Plongthongkum, N., Lutz, M., et al. (2012). The metabolome of induced pluripotent stem cells reveals metabolic changes occurring in somatic cell reprogramming. Cell Res. *22*, 168–177.

Peng, M., Yin, N., Chhangawala, S., Xu, K., Leslie, C.S., and Li, M.O. (2016). Aerobic glycolysis promotes T helper 1 cell differentiation through an epigenetic mechanism. Science *354*, 481–484.

Prieto, J., Leon, M., Ponsoda, X., Sendra, R., Bort, R., Ferrer-Lorente, R., Raya, A., Lopez-Garcia, C., and Torres, J. (2016). Early ERK1/2 activation promotes DRP1-dependent mitochondrial fission necessary for cell reprogramming. Nat. Commun. *7*, 11124.

Rajan, S., Jang, Y., Kim, C.H., Kim, W., Toh, H.T., Jeon, J., Song, B., Serra, A., Lescar, J., Yoo, J.Y., et al. (2020). PGE1 and PGA1 bind to Nurr1 and activate its transcriptional function. Nat. Chem. Biol. *16*, 876–886.

Ramaswamy, S., Nakamura, N., Vazquez, F., Batt, D.B., Perera, S., Roberts, T.M., and Sellers, W.R. (1999). Regulation of G1 progression by the PTEN tumor suppressor protein is linked to inhibition of the phosphatidylinositol 3-kinase/Akt pathway. Proc. Natl. Acad. Sci. U S A *96*, 2110–2115.

Shi, Y., Inoue, H., Wu, J.C., and Yamanaka, S. (2017). Induced pluripotent stem cell technology: a decade of progress. Nat. Rev. Drug Discov. *16*, 115–130.

Smiley, S.T., Reers, M., Mottola-Hartshorn, C., Lin, M., Chen, A., Smith, T.W., Steele, G.D., Jr., and Chen, L.B. (1991). Intracellular heterogeneity in mitochondrial membrane potentials revealed by a J-aggregate-forming lipophilic cation JC-1. Proc. Natl. Acad. Sci. U S A *88*, 3671–3675.

Sundaresan, N.R., Pillai, V.B., Wolfgeher, D., Samant, S., Vasudevan, P., Parekh, V., Raghuraman, H., Cunningham, J.M., Gupta, M., and Gupta, M.P. (2011). The deacetylase SIRT1 promotes membrane localization and activation of Akt and PDK1 during tumorigenesis and cardiac hypertrophy. Sci. Signal. *4*, ra46.

Takahashi, K., and Yamanaka, S. (2006). Induction of pluripotent stem cells from mouse embryonic and adult fibroblast cultures by defined factors. Cell *126*, 663–676.

Takahashi, K., and Yamanaka, S. (2016). A decade of transcription factor-mediated reprogramming to pluripotency. Nat. Rev. Mol. Cell Biol. *17*, 183–193.

Tanaka, A., and Youle, R.J. (2008). A chemical inhibitor of DRP1 uncouples mitochondrial fission and apoptosis. Mol. Cell *29*, 409–410.

Valente, A.J., Maddalena, L.A., Robb, E.L., Moradi, F., and Stuart, J.A. (2017). A simple ImageJ macro tool for analyzing mitochondrial network morphology in mammalian cell culture. Acta Histochem. *119*, 315–326.

Wan, X., and Helman, L.J. (2003). Levels of PTEN protein modulate Akt phosphorylation on serine 473, but not on threonine 308, in IGF-II-overexpressing rhabdomyosarcomas cells. Oncogene *22*, 8205–8211.

Wang, Y., Xu, C., Liang, Y., and Vanhoutte, P.M. (2012). SIRT1 in metabolic syndrome: where to target matters. Pharmacol. Ther. *136*, 305–318.

Warburg, O., Wind, F., and Negelein, E. (1927). The metabolism of tumors in the body. J. Gen. Physiol. *8*, 519–530.

Watanabe, S., Umehara, H., Murayama, K., Okabe, M., Kimura, T., and Nakano, T. (2006). Activation of Akt signaling is sufficient to maintain pluripotency in mouse and primate embryonic stem cells. Oncogene *25*, 2697–2707.

Williams, E.O., Taylor, A.K., Bell, E.L., Lim, R., Kim, D.M., and Guarente, L. (2016). Sirtuin 1 promotes deacetylation of Oct4 and maintenance of naive pluripotency. Cell Rep. *17*, 809–820.

Wong, D.J., Robert, L., Atefi, M.S., Lassen, A., Avarappatt, G., Cerniglia, M., Avramis, E., Tsoi, J., Foulad, D., Graeber, T.G., et al. (2014). Antitumor activity of the ERK inhibitor SCH772984 [corrected] against BRAF mutant, NRAS mutant and wild-type melanoma. Mol. Cancer *13*, 194.

Xu, K., Yin, N., Peng, M., Stamatiades, E.G., Shyu, A., Li, P., Zhang, X., Do, M.H., Wang, Z., Capistrano, K.J., et al. (2021). Glycolysis fuels phosphoinositide 3-kinase signaling to bolster T cell immunity. Science *371*, 405–410.

Yeung, F., Ramsey, C.S., Popko-Scibor, A.E., Allison, D.F., Gray, L.G., Shin, M., Kumar, M., Li, D., McCubrey, J.A., and Mayo, M.W. (2015). Regulation of the mitogen-activated protein kinase kinase (MEK)-1 by NAD(+)-dependent deacetylases. Oncogene *34*, 798–804.

Zhang, Z.N., Chung, S.K., Xu, Z., and Xu, Y. (2014). Oct4 maintains the pluripotency of human embryonic stem cells by inactivating p53 through Sirt1-mediated deacetylation. Stem Cells *32*, 157–165.

STAR★METHODS

KEY RESOURCES TABLE

REAGENT or RESOURCE	SOURCE	IDENTIFIER
Antibodies		
Rabbit anti-SIRT2	Abcam	Cat# ab51023; RRID: AB_882563
Rabbit anti-β-actin	Abcam	Cat# ab8227; RRID: AB_2305186
Mouse anti-HA tag	Abcam	Cat# ab1424; RRID: AB_301017
Rabbit anti-Phospho-DRP1(S616)	Cell Signaling Technology	Cat# 4494; RRID: AB_11178659
Rabbit anti-Phospho-DRP1(S637)	Cell Signaling Technology	Cat# 6319; RRID: AB_10971640
Rabbit anti-Phospho-p44/43 MAPK (ERK1/2) (Thr202/Tyr204)	Cell Signaling Technology	Cat# 4370; RRID: AB_2315112
Rabbit anti-Phospho-p38 MAPK (Thr180/Tyr182)	Cell Signaling Technology	Cat# 4511; RRID: AB_2139682
Rabbit anti-p38 MAPK	Cell Signaling Technology	Cat# 9218; RRID: AB_10694846
Rabbit anti-Phospho-EGFR (Tyr1068)	Cell Signaling Technology	Cat# 3777; RRID: AB_2096270
Rabbit anti-EGFR	Cell Signaling Technology	Cat# 4267; RRID: AB_2246311
Rabbit anti-Phospho-AKT (Thr308)	Cell Signaling Technology	Cat# 13038; RRID: AB_2629447
Rabbit anti-Phospho-AKT1 (Ser473)	Cell Signaling Technology	Cat# 9018; RRID: AB_2629283
Rabbit anti-Phospho-GSK-3α/β (Ser21/9)	Cell Signaling Technology	Cat# 8566; RRID: AB_10860069
Rabbit anti-GSK-3β	Cell Signaling Technology	Cat# 12456; RRID: AB_2636978
Rabbit anti-Acetylated-Lysine	Cell Signaling Technology	Cat# 9441; RRID: AB_331805
Goat anti-rabbit IgG	Cell Signaling Technology	Cat# 7074; RRID: AB_2099233
Alexa Fluor 488 donkey anti-mouse IgG (H+L)	Jackson ImmunoResearch Laboratories	Cat# 715-546-151; RRID: AB_2340850
Mouse anti-C-MYC	Roche	Cat# 11667149001; RRID: AB_390912
Mouse anti-TOM20	Santa Cruz Biotechnology	Cat# sc-17764; RRID: AB_628381
Mouse anti-DRP1	Santa Cruz Biotechnology	Cat# sc-101270; RRID: AB_2093545
Mouse anti-FIS1	Santa Cruz Biotechnology	Cat# sc-376447; RRID: AB_11149382
Mouse anti-MFF	Santa Cruz Biotechnology	Cat# sc-398617; RRID: AB_2744543
Mouse anti-MFN1	Santa Cruz Biotechnology	Cat# sc-166644; RRID: AB_2142616
Mouse anti-MFN2	Santa Cruz Biotechnology	Cat# sc-515647; RRID: AB_2811176
Mouse anti-AKT1	Santa Cruz Biotechnology	Cat# sc-5298; RRID: AB_626658
Mouse anti-ERK1/2	Santa Cruz Biotechnology	Cat# sc-514302; RRID: AB_2571739
Mouse anti-MEK1	Santa Cruz Biotechnology	Cat# sc-6250; RRID: AB_627922
Horse anti-mouse IgG	Vector Laboratories	Cat# PI-2000; RRID: AB_2336177
Chemicals, peptides, and recombinant proteins		
Seahorse XF calibrant solution	Agilent Technologies	Cat# 103059-100
Seahorse XF DMEM medium	Agilent Technologies	Cat# 103575-100
Immun-Blot PVDF Membrane	Bio-Rad Laboratories	Cat# 1620177
Quick Start™ Bradford dye reagent	Bio-Rad Laboratories	Cat# 5000205
Biolog MAS	Biolog	Cat# 72303
Biolog Redox Dye Mix MC	Biolog	Cat# 74353
Cell Lysis Buffer (10X)	Cell Signaling Technology	Cat# 9803
Matrigel® hESC-qualified matrix	Corning	Cat# 354277
GammaBind™ G Sepharose	GE Healthcare	Cat# 17-0885-01
NutriStem® hPSC XF medium	Sartorius	Cat# 05-100-1A
OSI-744	Selleckchem	Cat# S1023
PD0325901	Selleckchem	Cat# S1036

(Continued on next page)

Continued

REAGENT or RESOURCE	SOURCE	IDENTIFIER
Y-27632 2HCl	Selleckchem	Cat# S1049
SB202190	Selleckchem	Cat# S1077
SCH772984	Selleckchem	Cat# S7101
Mdivi-1	Selleckchem	Cat# S7162
L-ascorbic acid	Sigma-Aldrich	Cat# A4403
BCIP/NBT-blue liquid substrate	Sigma-Aldrich	Cat# B3804
D-glucose solution	Sigma-Aldrich	Cat# G8769
Nicotinamide	Sigma-Aldrich	Cat# N0636
Sodium butyrate	Sigma-Aldrich	Cat# 303410
Saponin	Sigma-Aldrich	Cat# SAE0073
Doxycycline hyclate	Sigma-Aldrich	Cat# D9891
3-(4,5-Dimethyl-2-thiazolyl)-2,5-diphenyl-2H-tetrazolium bromide (MTT)	Sigma-Aldrich	Cat# 475989
PolyJet™ transfection reagent	SignaGen Laboratories	Cat# SL100688
DMEM	Thermo Fisher	Cat# 11965092
DMEM/F-12	Thermo Fisher	Cat# 11320033
Fetal bovine serum (FBS)	Thermo Fisher	Cat# 26140079
KnockOut™ serum replacement	Thermo Fisher	Cat# 10828010
GlutaMAX™ supplement	Thermo Fisher	Cat# 35050061
MEM non-essential amino acids solution (NEAA)	Thermo Fisher	Cat# 11140050
Sodium pyruvate	Thermo Fisher	Cat# 11360070
β-mercaptoethanol (β-ME)	Thermo Fisher	Cat# 21985023
0.5M EDTA solution	Thermo Fisher	Cat# 15575020
DPBS	Thermo Fisher	Cat# 14190144
TrypLE™ express enzyme	Thermo Fisher	Cat# 12605028
FGF-Basic (AA 10-155) recombinant human protein	Thermo Fisher	Cat# PHG0023
Lipofectamine™ 2000 transfection reagent	Thermo Fisher	Cat# 11668019
4-12% Bis-Tris Plus gels	Thermo Fisher	Cat# NW04122BOX
Hoechst 33342	Thermo Fisher	Cat# H3570
TRIzol™ reagent	Thermo Fisher	Cat# 15596026
Critical commercial assays		
Seahorse XFp Cell Mito Stress Test Kit	Agilent Technologies	Cat# 103010-100
Seahorse XFp Real-Time ATP Rate Assay Kit	Agilent Technologies	Cat# 103591-100
QuickChange II XL Site-Directed Mutagenesis Kit	Agilent Technologies	Cat# 200522
BD Pharmingen™ FITC Annexin V Apoptosis Detection Kit	BD Biosciences	Cat# 556547
MitoPlate S-1	Biolog	Cat# 14105
iScript™ cDNA Synthesis Kit	Bio-Rad Laboratories	Cat# 1708891
SsoAdvanced™ Universal SYBR® Green Supermix	Bio-Rad Laboratories	Cat# 1725275
Citrate Colorimetric Assay Kit	BioVision	Cat# K655
Alpha-Ketoglutarate Colorimetric Assay Kit	BioVision	Cat# K677
Malate Colorimetric Assay Kit	BioVision	Cat# K637
Oxaloacetate Colorimetric Assay Kit	BioVision	Cat# K659
Proteome Profiler Human Phospho-Kinase Array Kit	R&D Systems	Cat# ARY003B
Venor GeM Mycoplasma Detection Kit	Sigma-Aldrich	Cat# MP0025

Continued

REAGENT or RESOURCE	SOURCE	IDENTIFIER
MitoProbe™ JC-1 Assay Kit	Thermo Fisher	Cat# M34152
Mitochondria Isolation Kit for Cultured Cells	Thermo Fisher	Cat# 89874
MitoTracker™ Green FM	Thermo Fisher	Cat# M7514
Novex™ ECL Chemiluminescent Substrate Reagent Kit	Thermo Fisher	Cat# WP20005
Direct-zol RNA MiniPrep Plus Kit	Zymo Research	Cat# R2072
Experimental models: Cell lines		
Human BJ newborn dermal fibroblasts	ATCC	Cat# CRL-2522; RRID: CVCL_3653
HEK293T/17 cells	ATCC	Cat# CRL-11268; RRID: CVCL_1926
Human adult dermal fibroblasts	Coriell Institute	Cat# GM03529; RRID: CVCL_7394
WA09 hESC	WiCell Institute	Cat# WA09; RRID: CVCL_9773
Oligonucleotides		
Primers used for qPCR, see Table S1		N/A
Recombinant DNA		
pcDNA3-Myr-HA-AKT1	Addgene	Cat# 9008; RRID: Addgene_9008
pMD2.G	Addgene	Cat# 12259; RRID: Addgene_12259
psPAX2	Addgene	Cat# 12260; RRID: Addgene_12260
OKSIM	Addgene	Cat# 24603; RRID: Addgene_24603
pcDNA3-HA-AKT1	Addgene	Cat# 73408; RRID: Addgene_73408
Non-targeting control siRNA pool	Horizon Discovery	Cat# D-001206-14-05
SMARTPool: Human DRP1 siRNA	Horizon Discovery	Cat# M-012092-01-0005
pLKO.1-SIRT2 shRNA (Clone ID: TRCN0000040218)	Horizon Discovery	Cat# RHS3979-201768981
pLKO.1-SIRT2 shRNA (Clone ID: TRCN0000040219)	Horizon Discovery	Cat# RHS3979-201768982
pLKO.1-SIRT2 shRNA (Clone ID: TRCN00000402200	Horizon Discovery	Cat# RHS3979-201768983
pLKO.1-SIRT2 shRNA (Clone ID: TRCN0000040221)	Horizon Discovery	Cat# RHS3979-201768984
pLKO.1-SIRT2 shRNA (Clone ID: TRCN0000010435)	Horizon Discovery	Cat# RHS3979-201797165
pLKO.1-SIRT2 shRNA (Clone ID: TRCN0000010436)	Horizon Discovery	Cat# RHS3979-201798782
pTRIPZ-SIRT2 shRNA (Clone ID: V2THS_240481)	Horizon Discovery	Cat# RHS4696-200673297
pTRIPZ-SIRT2 shRNA (Clone ID: V2THS_20091)	Horizon Discovery	Cat# RHS4696-200678567
pTRIPZ-SIRT2 shRNA (Clone ID: V3THS_367319)	Horizon Discovery	Cat# RHS4696-200771529
pTRIPZ-SIRT2 shRNA (Clone ID: V3THS_367315)	Horizon Discovery	Cat# RHS4696-200774606
pTRIPZ-SIRT2 shRNA (Clone ID: V3THS_367317)	Horizon Discovery	Cat# RHS4696-200775950
pTRIPZ-non-silencing shRNA control	Horizon Discovery	Cat# RHS4743
pGEM-T Easy vector	Promega	Cat# A1360
pcDNA3.1-Myc/His	Thermo Fisher	Cat# V80020
pcDNA3.1-Myc/His-MEK1	This paper	N/A
pcDNA3.1-Myc/His-MEK1-K175Q	This paper	N/A
pcDNA3.1-Myc/His-MEK1-K362Q	This paper	N/A
pcDNA3.1-HA-AKT1-K14R	This paper	N/A
pcDNA3.1-HA-AKT1-K20R	This paper	N/A

(Continued on next page)

Continued

REAGENT or RESOURCE	SOURCE	IDENTIFIER
Software and algorithms		
Seahorse Wave Desktop Software	Agilent Technologies	https://www.agilent.com
Image Lab™ software	Bio-Rad laboratories	https://www.bio-rad.com
FlowJo	Becton Dickinson & Company	https://www.flowjo.com
GraphPad Prism 8	GraphPad Software	https://www.graphpad.com/
Image J	National Institutes of Health	https://imagej.nih.gov/ij/
MiNA	Valente et al., 2017	https://github.com/StuartLab/MiNA
BioRender	BioRender	https://biorender.com

RESOURCE AVAILABILITY

Lead contact

Further information and requests for resources and reagents should be directed to and will be fulfilled by the Lead Contact, Kwang-Soo Kim (kskim@mclean.harvard.edu).

Materials availability

Cell lines generated and used in this study are available from the Lead Contact's laboratory upon request and following the completion of a Material Transfer Agreement.

Data and code availability

- All data reported in this paper will be shared by the lead contact upon request.
- This paper does not report original code.
- Any additional information required to reanalyze the data reported in this paper is available from the lead contact upon request.

EXPERIMENTAL MODEL AND SUBJECT DETAILS

Cell lines

Human BJ dermal fibroblasts (CRL-2522) and HEK293T/17 (CRL-11268) cells were purchased from ATCC and maintained in DMEM supplemented with 10% FBS, NEAA, and β-ME. GM03529 cells were obtain from Coriell Institute and maintained in DMEM supplemented 15% FBS, NEAA, and β-ME. WA09 hESCs were from WiCell Institute and maintained in NutriStem® hPSC XF medium. No cell lines used in this study are listed in the International Cell Line Authentication Committee (ICLAC) Register of Misidentified Cell Lines or the NCBI Biosample database of misidentified cell lines. All cell lines were authenticated by Interspecies Determination (Isoenzyme Analysis and STR analysis) by the providing company and were routinely tested for mycoplasma detection using a Venor GeM Mycoplasma Detection Kit (Sigma-Aldrich).

METHOD DETAILS

Plasmid construction

Human MEK1 coding sequence was PCR-amplified from BJ fibroblasts, then cloned into the pGEM-T Easy vector (Promega). The identity of MEK1 was confirmed by sequencing. Subsequently, MEK1 fragment was cloned into the pcDNA3.1-Myc/His vector (Thermo Fisher). Point mutations for MEK1 and AKT1 were generated by site-directed mutagenesis using a QuickChange II XL Site-Directed Mutagenesis Kit (Agilent Technologies).

Lentivirus production

Lentiviral vectors were co-transfected with packaging plasmids into 293T cells, maintained in DMEM supplemented with 10% FBS, using PolyJet transfection reagent according to the manufacturer's instruction. Supernatants containing lentiviruses were harvested 48 h after transfection and filtered using 0.45 μm Millex-hV (Millipore) filters to remove cell debris.

Live cell metabolic analysis

Oxygen consumption rate (OCR) and extracellular acidification rate (ECAR) were measured using the Seahorse XFp analyzer (Agilent Technologies) according to the manufacturer's instruction. Briefly, cells were plated onto wells of a XFp cell culture miniplate and incubated in a 37°C CO_2 incubator overnight. The assay was performed after cells were equilibrated for 1 h in XF assay medium

supplemented with 10 mM D-glucose, 5 mM sodium pyruvate, and 2 mM glutamax in a non-CO$_2$ incubator. Mitochondrial activity was monitored through sequential injections of 1 μM oligomycin, 2 μM FCCP and 0.5 μM rotenone/antimycin A to calculate basal respiration (baseline OCR – rotenone/antimycin A OCR), maximal respiration (FCCP OCR – rotenone/antimycin A OCR), ATP turnover (baseline OCR – oligomycin OCR), and oxidative reserve (maximal respiration – basal respiration). ATP production rate was measured using the Seahorse XFp Real-Time ATP Rate Assay Kit (Agilent Technologies) following the manufacturer's instruction. Each plotted value was normalized to total protein quantified using a Bradford protein assay (Bio-Rad Laboratories) and analyzed using the Seahorse WAVE Desktop software (Agilent Technologies).

Measurement of mitochondrial length
Cells were washed twice with PBS and fixed with 4% formaldehyde in PBS (pH 7.4) for 10 min. Cells were incubated for 30 min in blocking solution (0.1% Triton X-100 and 1% horse serum in PBS) at room temperature. Cells were incubated with anti-TOM20 antibody (Santa Cruz Biotechnology, sc-17764, 1:100) in PBS containing 0.1% Triton X-100 and 1% horse serum overnight. Cells were then incubated with Alexa Fluor 488-conjugated, donkey anti-mouse IgG antibody (Jackson ImmunoResearch Laboratories, 715-546-151, 1:1000) with Hoechst 33342 (Thermo Fisher) for nuclei staining at room temperature for 1 h. Cell images were obtained by confocal microscopy (KEYENCE, Osaka, Japan). Mitochondrial length was analyzed using MiNA software (Valente et al., 2017).

Mitochondrial function assay
Mitochondrial function assays were performed using the MitoPlate S-1 (Biolog) following the manufacturer's instruction. Briefly, cells treated with doxycycline for 3 days were harvested and resuspended in 1x Biolog MAS solution containing 1x Redox Dye MC and saponin. Cell mixture was dispensed onto wells of the MitoPlate S-1 and plates were sealed with breathable membranes and incubated in a 37°C CO$_2$ incubator. After 1 h incubation, OD595 was measured on a Synergy HT BioTek microplate reader (BioTek Instruments).

Measurement of mitochondrial metabolites
Mitochondrial metabolites including citrate, α-ketoglutarate, malate, and oxaloacetate were measured using a colorimetric assay kit (all from Biovision) following the manufacturer's instruction.

Measurement of mitochondrial membrane potential
The mitochondrial membrane potential was measured using the JC-1 cationic dye (5,5',6,6'-tetrachloro-1,1',3,3'-tetraethylbenzimidazolylcarbocyanine iodide; Thermo Fisher), which stains live cells in a membrane potential-dependent fashion: green fluorescence (λ_{em} = 525 nm) is emitted by JC-1 monomers and red fluorescence (λ_{em} = 590 nm) by JC-1 aggregates. Briefly, cells were washed twice with cold PBS and then stained with the JC-1 (10 μg/ml) dye for 10 min at 37°C; green (FL-1) and red (FL-2) were measured by a BD Accuri flow cytometer.

Measurement of mitochondrial mass
The mitochondrial mass was measured using the MitoTracker™ Green FM (Thermo Fisher) according to the manufacturer's instruction. Briefly, cells were washed twice with cold PBS, stained with the MitoTracker™ Green FM (25 μg/ml) for 10 min at room temperature and then measured by a MACS Quant 16 analyzer (Miltenyi Biotec).

Transmission electron microscopy
Cells were fixed in 2.5% glutaraldehyde, 2% formaldehyde, 0.5 mg/ml calcium chloride, 0.1M sucrose in 0.1M sodium cacodylate (pH 7.4) for 1 h and post-fixed with 1% osmium tetroxide for 30 min. Fixed cells were dehydrated in graded ethanol series and anhydrous acetone, followed by infiltration and embedding in Embed 812/Araldite 502 resin. After polymerization, cells were sectioned in ultra-thin slices (70 nm) collected on Formvar-coated copper slot grids, then post-stained with uranyl acetate and Reynold's lead citrate. The sections were imaged on a JEOL JEM-1200 EX II electron microscope (Jeol Technics Ltd., Tokyo, Japan) equipped with a 1k charged-coupled device camera.

Isolation of cytosolic and mitochondrial fractions
Cytosolic and mitochondrial fractions were isolated from cultured cells using a mitochondria isolation kit (Thermo Fisher) according to the manufacturer's instruction.

Phospho-kinase array
Phospho-kinase array was performed using a Human Phospho-Kinase Array Kit (R&D Systems) according to the manufacturer's instruction.

qRT-PCR
Total RNA was extracted from cells by using the Direct-zol RNA MiniPrep Plus kit (Zymo Research) and cDNA was synthesized using the iScript cDNA Synthesis Kit (Bio-Rad Laboratories). For quantitative analyses, qRT-PCR were performed using SsoAdvanced

SYBR Green supermix (Bio-Rad Laboratories) with target genes specific primers. The expression level of each gene is shown as a relative value following normalization against that of the β-actin gene. Primers used in this study are listed in Table S1.

Immunoprecipitation

For immunoprecipitation assays, cell lysates were incubated with specific antibodies against MEK1 (Santa Cruz Biotechnology, sc-6250, 1:100), ERK1/2 (Santa Cruz Biotechnology, sc-514302, 1:100), AKT1 (Santa Cruz Biotechnology, sc-5298, 1:100) or DRP1 (Santa Cruz Biotechnology, sc-101270, 1:100) at 4°C overnight. After addition of Gammabind G Sepharose beads, samples were incubated at 4°C for 4 h. Beads were washed three times with cold PBS and proteins were released from the beads by boiling in SDS-sample loading buffer and analyzed by SDS-PAGE.

Immunoblotting

Cells were washed with PBS twice and lysed in 1x Cell Lysis Buffer (Cell Signaling Technology). The cell lysates were loaded onto 4-12% Bis-Tris Plus gels (Thermo Fisher) and separated by electrophoresis followed by transfer onto a piece of Immun-Blot PVDF membrane (Bio-Rad Laboratories). After blocking with 5% (w/v) skim milk in PBST (PBS containing 0.05% Tween-20) for 30 min, membranes were incubated overnight at 4°C with primary antibodies. Membranes were washed three times with PBST and then incubated for 1 h with horseradish peroxidase-conjugated secondary antibodies. After washing three times with PBST, bound antibodies were detected by chemiluminescence using the Novex™ ECL Chemiluminescent Substrate Reagent Kit (Thermo Fisher). For immunoblotting, anti-SIRT2 (Abcam, ab51023, 1:1000), anti-phospho-DRP1 (S616) (Cell Signaling Technology, 4494, 1:500), anti-phospho-DRP1 (S637) (Cell Signaling Technology, 6319, 1:500), anti-DRP1 (Santa Cruz Biotechnology, sc-101270, 1:1000), anti-FIS1 (Santa Cruz Biotechnology, sc-376447, 1:1000), anti-MFF (Santa Cruz Biotechnology, sc-398617, 1:1000), anti-MFN1 (Santa Cruz Biotechnology, sc-166644, 1:1000), anti-MFN2 (Santa Cruz Biotechnology, sc-515647, 1:1000), anti-TOM20 (Santa Cruz Biotechnology, sc-17764, 1:1000), anti-phospho-ERK1/2 (Cell Signaling Technology, 4370, 1:500), anti-ERK1/2 (Santa Cruz Biotechnology, sc-514302, 1:1000), anti-phospho-p38 (Cell Signaling Technology, 4511, 1:500), anti-p38 (Cell Signaling Technology, 9218, 1:1000), anti-phospho-EGFR (Cell Signaling Technology, 3777, 1:500), anti-EGFR (Cell Signaling Technology, 4267, 1:1000), anti-phospho-AKT (Thr308) (Cell Signaling Technology, 13038, 1:500), anti-phospho-AKT1 (Ser473) (Cell Signaling Technology, 9018, 1:500), anti-AKT1 (Santa Cruz Biotechnology, sc-5298, 1:1000), anti-phospho-GSK3α/β (Cell Signaling Technology, 8566, 1:500), anti-GSK3β (Cell Signaling Technology, 12456, 1:1000), anti-acetylated-Lysine (Cell Signaling Technology, 9441, 1:1000), anti-MEK1 (Santa Cruz Biotechnology, sc-6250, 1:1000), anti-MYC (Roche, 11667149001, 1:1000), anti-HA (Abcam, ab1424, 1:1000), and anti-β-actin (Abcam, ab8227, 1:1000) antibodies were used as primary antibodies. The secondary antibodies were horseradish peroxidase-conjugated, goat anti-rabbit IgG (Cell Signaling Technology, 7074, 1:1000) and horse anti-mouse IgG (Vector Laboratories, PI-2000, 1:2000).

Annexin V staining

For apoptosis analysis, cells were washed twice with cold PBS, and then stained with Annexin V-FITC and propidium iodide (BD Biosciences) and analyzed by flow cytometer.

Cell viability assay

Cell viability assays were performed using 3-(4,5-Dimethyl-2-thiazolyl)-2,5-diphenyl-2H-tetrazolium bromide (MTT; Sigma-Aldrich) as described previously (Rajan et al., 2020). Briefly, cells were incubated with 15 μl of MTT solution (5 mg/ml in DPBS) for 3.5 h. MTT crystals were dissolved in 150 μl of MTT solvent (4 mM HCl and 0.1% Nonidet P-40 in isopropanol) and the generated amount of blue formazan was determined spectrophotometrically at 570 nm.

Human iPSC formation assay

Human iPSCs were generated using lentiviral particles from OSKIM vector to introduce the OSKM factors (OCT4, SOX2, KLF4, and C-MYC) into fibroblasts. ESC-like colonies were formed after 2 weeks of viral infection and fixed cells were stained with a solution of the alkaline phosphatase substrate NBT/BCIP followed by three washes with PBS to stop the reaction.

QUANTIFICATION AND STATISTICAL ANALYSIS

All statistical analyses were performed using the GraphPad Prism 8 software. Obtained data were statistically analyzed using paired Student's t-test and one- or two-way ANOVA test with Tukey's post-test, and the graphs show the mean ± SD. P values are indicated by asterisks with: *$p<0.05$; **$p<0.01$; ***$p<0.005$.